ELSEVIER

Contents lists available at ScienceDirect

Chemical Engineering Journal

journal homepage: www.elsevier.com/locate/cej





Enhancing nitrate reduction reaction electroactivity of Fe single atom catalyst by modification of Fe nanoclusters and further application in self-powered ammonia synthesis from air

Bingyi Song ^{a,b,1}, Dong Xiang ^{c,1}, Chengjie Chen ^d, Jinchang Xu ^e, Yangshuai Ma ^a, Linjing Yang ^b, Ming-Hsien Lee ^f, DengkeZhao ^{a,g,*}, Kai Han ^{d,**}, Nan Wang ^{d,**}

- ^a School of Materials Science and Engineering, Henan Normal University, Xinxiang, Henan 453007, China
- b National Engineering Research Center of Vacuum Metallurgy, Kunming University of Science and Technology, Kunming 650093, China
- ^c College of chemistry and materials engineering, Bohai University, Jinzhou 121013, China
- d Siyuan Laboratory, Guangzhou Key Laboratory of Vacuum Coating Technologies and New Energy Materials, Guangdong Provincial Engineering Technology Research Center of Vacuum Coating Technologies and New Energy Materials, Guangdong Provincial Key Laboratory of Nanophotonic Manipulation, Department of Physics, Jinan University, Guangzhou 510632, China
- ^e Guangdong Provincial Key Laboratory of Terahertz Quantum Electromagnetics, GBA Branch of Aerospace Information Research Institute, Chinese Academy of Sciences, Guangzhou 510700, Guangdong, China
- f Department of Physics, Tamkang University, New Taipei 25137, Taiwan
- ⁸ School of Physics, Henan Normal University, Xinxiang, Henan 453007, China

ARTICLE INFO

Keywords: Single atom electrocatalyst $Fe_{NC}/Fe-N_x$ NO_3RR Ammonia synthesis Triboelectric nanogenerator

ABSTRACT

Designing cost-effective nitrate reduction reaction (NO_3RR) electrocatalysts and exploring a clean and sustainable energy as power to drive this process are of great significance for the sustainability of the nitrogen cycle. Herein, by direct pyrolysis of MOF and $g\cdot C_3N_4$, an efficient electrocatalyst with Fe nanoclusters (Fe_{NC}) modified Fe single atoms ($Fe_{NC}/Fe\cdot N_x$) was prepared for NO_3RR . Characterizations and theoretical calculations indicate that the Fe_{NC} effectively regulates the d-band structure of Fe sites, increasing the electron occupation in d_{z2} orbital to optimize the bond order (BO) for intermediates, thus lowering the energy barrier of rate-determining step (RDS: $NHO^* + H^+ + e^- \rightarrow N^* + H_2O$). Therefore, the $Fe_{NC}/Fe\cdot N_x$ exhibits remarkable NO_3RR performance with a high faradaic efficiency (FE) of 93.6 % at -0.9 V vs. RHE and an excellent NH_3 yield rate of 30.87 mg h^{-1} mg $_{cal}^{-1}$ at -1.1 V vs. RHE. Based on these, an updated triboelectric nanogenerator-based self-powered NH_3 synthesis system was presented, and a high rate of 22.66 μ g h^{-1} was achieved directly using air as the raw material. This work provides a simple strategy to enhance NO_3RR performance of $Fe\cdot N_x$ electrocatalysts, and further demonstrates a smart and sustainable way for NH_3 synthesis.

1. Introduction

 NH_3 is an indispensable feedstock in modern agriculture, serving as a key ingredient in the production of nitrogenous fertilizers [1–3]. Moreover, it is also regarded as a prospective alternative fuel source due to its high energy density (4.3 kWh kg $^{-1}$) and zero-carbon emission profile [4,5]. The Haber-Bosch process is currently the predominant method to produce NH_3 in industrial settings, but the inherent harsh reaction conditions associated with this process result in significant

energy consumption and CO_2 emissions [6–9]. In contrast, the electrochemical synthesis of NH_3 driven by electricity opens up a mild condition to produce NH_3 , and it can be coupled with renewable energy sources (such as wind and solar) [10,11]. Among them, the electrochemical reduction of NO_3 to NH_3 is an ideal way, which not only enables the production of NH_3 with zero-emission, but also effectively eliminates NO_3 from sewage [12,13]. However, there are some issues that must be addressed to ensure an efficient, clean, and sustainable synthesis of NH_3 during NO_3RR . One is that NO_3RR involves an $8e^-$

^{*} Correspondence to: D. Zhao, School of Materials Science and Engineering, Henan Normal University, Xinxiang, Henan 453007, China.

^{**} Corresponding authors.

E-mail addresses: zhaodengke@htu.edu.cn (DengkeZhao), kaihan54@jnu.edu.cn (K. Han), nanwang@email.jnu.edu.cn (N. Wang).

 $^{^{1}\,}$ These authors contributed equally to this work.

transfer process accompanied by the formation of multiple intermediates, thereby requiring high active and selective electrocatalysts [14–18]. Another is how to power NO_3RR to product NH_3 by clean electric energy at any given time and in any given location, which necessitates the development of further innovative electrochemical synthesis devices.

Single atom dispersed Fe-N_x catalysts possess the main activity sites of Fe center coordinated with four N atoms, and are regarded as a class of the most cost-effective electrocatalysts for NO₃RR due to the strengths of high atomic utilization and low-cost [19-24]. For example, Wu et al. reported a Fe-N_x electrocatalysts for NO₃RR, which demonstrated a high FE of 75 % and an NH₃ yield rate (0.46 mmol h^{-1} cm⁻²) [25]. Nevertheless, the single active site and symmetrical electronic density distribution in Fe-N_x prevent the atalytic performance to some extent [26–28]. Similar to the active single atoms in the catalyst, nanocluster (NC) also has high atomic utilization, therefore reasonable combination with NC maybe a feasible strategy to enrich the active sites of single atom catalyst (SAC). Furthermore, several relevant studies have demonstrated that the introduction of NC can modulate the electronic structure (electron filling and spin state) of metal-nitrogen-carbon (M-N_x) to break the symmetrical electronic distribution, which contributes to the enhancement of the electrocatalytic performance [29–31]. For example, Huang et al. demonstrated that the modification of nano cluster can alter the TM-N bond lengths, thereby facilitating the desorption of intermediates during the ORR process [32]. Inspired by these, the introduction of NC may represent a rational approach to enhancing NO₃RR electroactivity and selectivity of Fe-N_x. Moreover, combining with systematic characterization and theoretical analysis to clarify the elucidation of the relationship between electron structure (spin state) and activity holds considerable promise for the further advancement of Fe-N_x in NO₃RR.

In addition to an excellent electrocatalyst, an eco-friendly controllable raw material source, a sustainable clean energy, and their reasonable utilizations are tremendous priorities to meet the needs of future applications. Just like the nitrogen cycle in nature, a cost-effective and easy method to get NO₃ is discharge in the air. Over the past decade, triboelectric nanogenerator (TENG), has been a rising star in energy field [33-35]. By using a wide range of materials and simple fabricating, TENG can harvest various environmental mechanical energy into electric energy [36-38]. Among its main application directions, used as a high-voltage source particularly provides an efficient and low-cost method to build a strong electric field for air discharge and following NO₃ forming, which can be further used in NO₃RR [39,40]. Meanwhile, TENG is also easy to obtain high current and enough voltage for driving electroreduction reactions by reasonable structure designing and circuit management [41]. Thus, with the simple combination of an efficient catalyst and TENGs, it is a promising way to fabricate an air-sourced selfpowered ammonia synthesis system for promoting NO₃RR applications.

Herein, $Fe_{NC}/Fe-N_x$ is prepared as a NO_3RR electrocatalyst by a simple pyrolysis strategy using Fe-ZIF-8 and $g-C_3N_4$ as precursors. Characterizations and density functional theory (DFT) analysis demonstrate that the $g-C_3N_4$ as thermal removal template is capable of etching carbon substrate to enrich the micro/mesoporous structures and increase the specific surface area, thereby helping to expose more active sites and boost the mass/electron transfer. The in-situ formed Fe_{NC} enhances the filling of electrons in the d_{Z2} orbital of Fe sites and increases their spin state, thereby optimizing the bond order (BO) between intermediates and active sites during NO_3RR to reduce the Gibbs free energy barrier (ΔG) of the rate-determining step (RDS). Therefore, the $Fe_{NC}/Fe-N_x$ exhibits an enhanced NO_3RR performance, including a high faradaic efficiency (FE) of 93.6 % at -0.90 V (vs. RHE) and an excellent NH_3 yield rate (30.87 mg h^{-1} mg $_{cat}^{-1}$) at -1.10 V, much superior to Fe- N_x (82 %, 19.83 mg h^{-1} mg $_{cat}^{-1}$).

Furthermore, the Fe $_{NC}/{\rm Fe-N}_x$ was employed in an updated self-powered NH $_3$ synthesis system based on TENGs. With this system, NH $_3$ is efficiently synthesized from air with a high yield rate of 22.66 μg

 $h^{-1}.$ Additionally, a rechargeable Zn-NO $_3$ battery based on the Fe $_{NC}/{\rm Fe-N}_x$ also shows excellent performance, with a high-power density peak (7.54 mW cm $^{-2}$) and long-term stable charge/discharge cycle (100 $h@2.0\,$ mA cm $^{-2}$). These studies well demonstrate the application prospects of Fe $_{NC}/{\rm Fe-N}_x$.

2. Experimental section

2.1. Preparation of ZIF-8 and Fe-ZIF-8

ZIF-8 nanoparticles (NPs) were prepared by previously reported method but with a few changes [42]. Firstly, 8.0 mmol $\rm Zn(NO_3)_2$ was dissolved in 200 mL methanol to form A solution, 64.0 mmol 2-dimethylimidazole (2-MIM) was added to another 200 mL methanol to form B solution. Then, the B solution was poured into the A solution with quickly stirring at room temperature for 20 min. After aging for 24 h, the ZIF-8 NPs were washed with ethanol 3 times and obtained by centrifugation. Fe doped ZIF-8 NPs were prepared by the same process as ZIF-8 except for the addition of 1.5 and 2.5 mmol FeCl₂ solutions, named Fe_{1.5}-ZIF-8 and Fe_{2.5}-ZIF-8 respectively.

2.2. Preparation of Fe-N_x and Fe_{NC}/Fe-N_x

First, 100 mg of Fe $_{2.5}$ -ZIF-8 was dispersed in 100 mL of methanol by ultrasound for 10 min. Then, 500 mg of g-C $_3$ N $_4$ was added in the solution with another 30 min ultrasonic processing. The products were obtained by wash and filtration, named Fe $_{2.5}$ -ZIF-8/g-C $_3$ N $_4$. Finally, Fe $_{2.5}$ -ZIF-8/g-C $_3$ N $_4$ was placed in a tubular furnace and annealed for 2 h at 900 °C in N $_2$ atmosphere to prepare Fe $_{NC}$ modified Fe single atom catalyst, named Fe $_{NC}$ /Fe-N $_x$. As a comparison, Fe-N $_x$ was prepared by direct heat treatment of Fe $_{1.5}$ -ZIF-8/g-C $_3$ N $_4$. To analyze the effects of g-C $_3$ N $_4$, Fe $_{2.5}$ -ZIF-8-HT also prepared by direct heat treatment of Fe $_{2.5}$ -ZIF-8.

2.3. Materials characterization

Scanning electron microscopy (SEM) (Zeiss, Germany) and transmission electron microscopy (TEM) (Zeiss, Germany) were carried out to observe the morphology and structure of as-prepared samples. Highangle annular dark field-scanning transmission electron microscopy (HAADF-STEM) (FEI, Netherlands) were carried out to determinate single atoms. X-ray diffraction (XRD) (Bruker D8) and Raman (LabRAM HR Evolution) were performed to analyze the crystalline phase and carbon structure. Brunauer—Emmet—Telle (BET) measurement (QuantachromeAutosorb-iQ-TPX instrument) was used to evaluate specific surface area and the porous structure. X-ray absorption spectroscopy (XAS) (Beijing Synchrotron Radiation Facility) was used to analyze the coordination environment and structure of Fe atoms.The XPS tests are carried out through Phi X-tool instrument, and the data are fitted by XPSpeak41 Software, and the binding energies are calibrated by C 1 s (284.6 eV).

2.4. Electrochemical measurements

The electrochemical tests were performed on a CHI 760e workstation through a three-electrode configuration, in which catalyst modified carbon paper, Ag/AgCl electrode and Pt sheet were used as work electrode, reference electrode and counter electrode, respectively. The loading of catalyst was 0.4 mg cm $^{-2}$. Linear sweep voltammetry (LSV) curves were tested in 0.50 M NaNO $_3/0.10$ M $\rm K_2SO_4$ mixed electrolyte at potential between 0.0 V and - 1.60 V vs. RHE with a scan rate of 5 mV s $^{-1}$. Alternating current (AC) impedance was recorded within a frequency range of 0.01 Hz to 100 kHz at an amplitude of 10 mV. Chronopotentiometry was tested at different potential (-0.60 to -1.10 V vs. RHE).

The FE of NH₃ and NO₂ conversion was calculated as follows:

$$FE_{NH_3} = \left\lceil \left(8 \times 10^{-6} \times F \times c(NH_3) \times V\right) / Q \right\rceil \times 100\%$$

$$\text{FE}_{\text{NO}_2}{}^- = \left[\left(2 \times 10^{-6} \times \text{F} \times \text{c(NO}_2{}^-) \times \text{V} \right) \middle/ Q \right] \times 100\%$$

The NH_3 yield rate (Y_{NH3}) was calculated using the following equation:

$$Y_{NH_3} (mg h^{-1} mg_{cat}^{-1}) = [c(NH_3) \times V \times 17]/10 (t \times mg_{cat})$$

where Q (C) is the quantity of applied electricity, F is the Faraday constant (96485C mol^{-1}), $\text{c(NH}_3)$ and $\text{c(NO}_2^-)$ (umol L^{-1}) are the generated concentration of NH₃ and NO $_2^-$, V (L) is the volume of electrolyte in the cathode cell, t (h) is the reaction time.

2.5. Determination of NH₃

The modified indophenol blue method was used to quantify concentration of NH $_3$. First, a certain amount of electrolyte after test was taken out, and diluted to the detection range. Then, 2 mL 1 M NaOH solution with containing of 5 wt% $C_7H_6O_3$ and 5 wt% $C_7H_5O_3N_8$ was added into the 2 mL diluted electrolyte. Subsequently, 1 mL 0.05 M NaClO solution and 0.2 mL 1.0 wt% Na $_2$ [Fe(CN) $_5$ NO]· $_4$ O were added into the above solution and mixed uniformly. The absorption intensity of 655 nm was recorded after keeping in the dark place for 2 h. The related concentration-absorbance curve was obtained by a series of NH $_4$ Cl solutions.

2.6. Determination of NO₂

A certain amount of electrolyte from the cathode chamber was taken and diluted to the detection range. Then, 100 μL of chromogenic agent was added into the diluted electrolyte and mixed uniformly. The absorption intensity of 540 nm was recorded after keeping for 20 min. The related concentration-absorbance curve was recorded from a series of NaNO2 solutions.

2.7. ¹⁵N isotope labeling

To determine the source of NH_3 during the reaction process, a ^{15}N isotope labeling experiment was carried out by using $0.10~M~K_2SO_4 + 0.50~M~Na^{15}NO_3$ as the electrolyte. The reaction products were gathered after 1800~s at -0.90~V vs. RHE, then identified by ^{1H}NMR measurement.

2.8. NMR measurement

600~uL of the tested solution, 25~uL of $1.0~M~H_2SO_4$ solution, 50~uL of DMSO- d_6 and 0.0044~g of maleic acid were mixed sufficiently, and then transferred to the NMR tube. The ^{1H}NMR specra are obatined by the NOESY method (NS = 8,D1 = 1 s, D8 = 0 s, P1 = 10 us, SW = 20.02 ppm, AQ = 2.73 S, TD = 65.54 k, O1P = 6.175 ppm) [43,44]. To quantified the content of NH3, the $^{15}NH_4Cl$ solution with different concentrations (2.0, 4.0, 6.0, 8.0 and 10.0 mmol L^{-1}) were also anlyzed by the same way to bulid the standard curve of $^{15}NH_4^+$ concentration and integral area.

2.9. DFT calculation

Density functional theory (DFT) calculations were performed using Pseudopotential Plane-wave (PP-PW) method in the castep code of Materials Studio 2019. The general gradient approximation (GGA) and Perdew-Burke-Ernzerhof (PBE) were chosen for the exchange-correlation energy, and OTFG ultrasoft pseudopotential were used for the core electrons. The kinetic cutoff energy, the convergence in the energy and forces were set to 500 eV, 1×10^{-5} eV per atom and 0.03 eV $\rm \mathring{A}^{-1}$, respectively. A layer of the FeN4 structure on the graphite was

modeled and compounded with a cluster composed of 5 Fe atoms, and the vacuum space was selected at 20 Å. For the geometrical structure optimization, $3\times 3\times 1$ of Monkhorst-Pack k-mesh was employed and the self-consistent field tolerance and the maximum translation were set to be 1×10^{-5} eV and 1×10^{-3} Å, respectively. The adsorption energy (ΔE) was calculated by the formula as follow:

$$\Delta E = E_{adsorbate+slab} - E_{adsorbate} - E_{slab}$$

where $E_{adsorbate+slab}$, $E_{adsorbate}$, and E_{slab} represent the total energy of the adsorbate binding with the slab, the energy of the adsorbate in the gas phase and the bare slab, respectively.

And the Gibbs free energy change (ΔG) of an elementary reaction was calculated by $\Delta G = \Delta E + \Delta ZPE$ - $T\Delta S$, in which ΔZPE and ΔS represent zero-point energy and entropy change, respectively.

2.10. Fabrication and measurements of the multi-disk TENGs

Based on the previous work [40], the vertical multi-disk TENGs are composed of printed circuit board based stators (stator-8 and stator-32), corresponding epoxy glass fiber disk board (20 cm, 0.3 mm) based rotors (rotor-8 and rotor-32) covered with Kapton films (60 μ m), and symmetrical artificial wool brushes for triboelectrification with the Kapton films. A direct current motor was used to supply the simulated mechanical energy (\sim 1600 rpm). The performance was measured by an electrometer (6514, Keithley) and a multimeter (P186, Pintech) with a high-voltage probe (HVP-40, 1 G Ω).

2.11. Simulated air discharge and electrocatalytic experiments

The discharge devices are fabricated by steel needles and Tantalum sheets with different interelectrode distances (0.5 mm, 1 mm, 2 mm, 3 mm). Polymethyl methacrylate (PMMA) boxes (4 cm \times 4 cm \times 4 cm) were used as the container. Air source was supplied by a mini vacuum pump. The air flow was washed by H_2SO_4 (0.05 M) and NaOH (0.05 M) solutions, then it went through the discharge device, and finally was inlet into the cathode chamber containing pure water (25 mL). After 1 h air discharge driven by rectified TENG-a, the concentrations of NO_3^- and NO_2^- were measured by quick water-analysis-strips (24 Pro Scan, JBL).

The electrocatalytic experiments was carried out in a H-shape electrolytic cell with the mixed electrolyte of 0.50 M $\mathrm{NO_3^-}/0.10$ M $\mathrm{K}_2\mathrm{SO}_4$. The working electrode and counter electrode were carbon paper with catalyst (5.9 mg cm $^{-2}$) and Pt sheet electrode, respectively. A series of transformers and a rectifier were tested to help manage the output of TENG-b. At the optimum ratio, the electrolytic cell was driven by TENG-b for 1 h electrocatalytic reaction. The concentration of NH $_3$ was measured with proper dilution treatment by using the same method.

2.12. Self-powered ammonia synthesis from air

First, a range of K_2SO_4 solutions were tested for the selection of optimum electrolyte. Then, the same optimization process of transformer ratio was performed. With the simulated mechanical energy power, the ammonias synthesis system ran for 2 h using air as the raw material. The concentration of ammonia was measured by using the same method.

2.13. The measurement of rechargeable Zn-NO₃ battery

Rechargeable Zn-NO $_3$ battery was tested by H-type electrolytic cell separated by Nafion membrane through two electrode system using Zn Foil and Fe $_{\rm NC}$ /Fe-N $_{\rm N}$ modified carbon paper (CP) (geometric area: 1.0 cm $^{-2}$) as anode and cathode, 3.5 M NaOH/0.25 M NaNO $_3$ solution as electrolyte respectively. The polarization and open-circuit voltage curves were tested by CHI 760D workstation. The long-term charge/discharge cycle measurement was carried out by Land CT2001A at 2.0

 ${
m mA~cm^{-2}}$, each cycle is 20 min, charge for 10 min, then discharge for 10 min.

3. Results and discussion

Fig. 1a illustrates the synthetic process of $Fe_{NC}/Fe-N_x$, more details can be seen in experimental section. The synthesis commenced with the preparation of Fe-ZIF-8 through the self-assembly of 2-dimethylimidazole (2-MIM) and $Zn(NO_3)_z/FeCl_2$, and then Fe-ZIF-8 was mixed with g-C₃N₄ to prepare Fe-ZIF-8/g-C₃N₄. Subsequently, the Fe_{NC}/Fe-N_x composite was obtained through the annealing of the Fe-ZIF-8/g-C₃N₄ at 900 °C under N₂ for 2 h. XRD patterns were employed to examine the alteration of the crystal phase structure throughout the synthesis of the samples. As shown in Fig. S1, where one can find clear the precursors

can maintain ZIF-8 phase well before and after doping Fe. After annealing, the characteristic diffraction peaks of ZIF-8 are completely disappear, while a broad characteristic peak at about 25° can be found (Fig. 1b), corresponding to graphitic carbon (002) [45]. Moreover, no discernible peak associated with a particular Fe species is evident, suggesting that Fe may exist in the form of either single atoms or nanoclusters.

To gain deeper insight into the structural characteristics of the asprepared samples, the Raman and BET measurements were conducted. Fig. 1c reveals that the as-made samples possess similar degree of graphitization, the ratios between D band and G band of Fe_{2.5}-ZIF-8-HT, Fe-N_x and Fe_{NC}/Fe-N_x are 1.18, 1.28 and 1.23 respectively. As illustrated in Fig. 1d, the N₂ adsorption-desorption isotherms reveal that Fe_{NC}/Fe-N_x (1209.6 m² g⁻¹) and Fe-N_x (1270.83 m² g⁻¹) exhibit a markedly

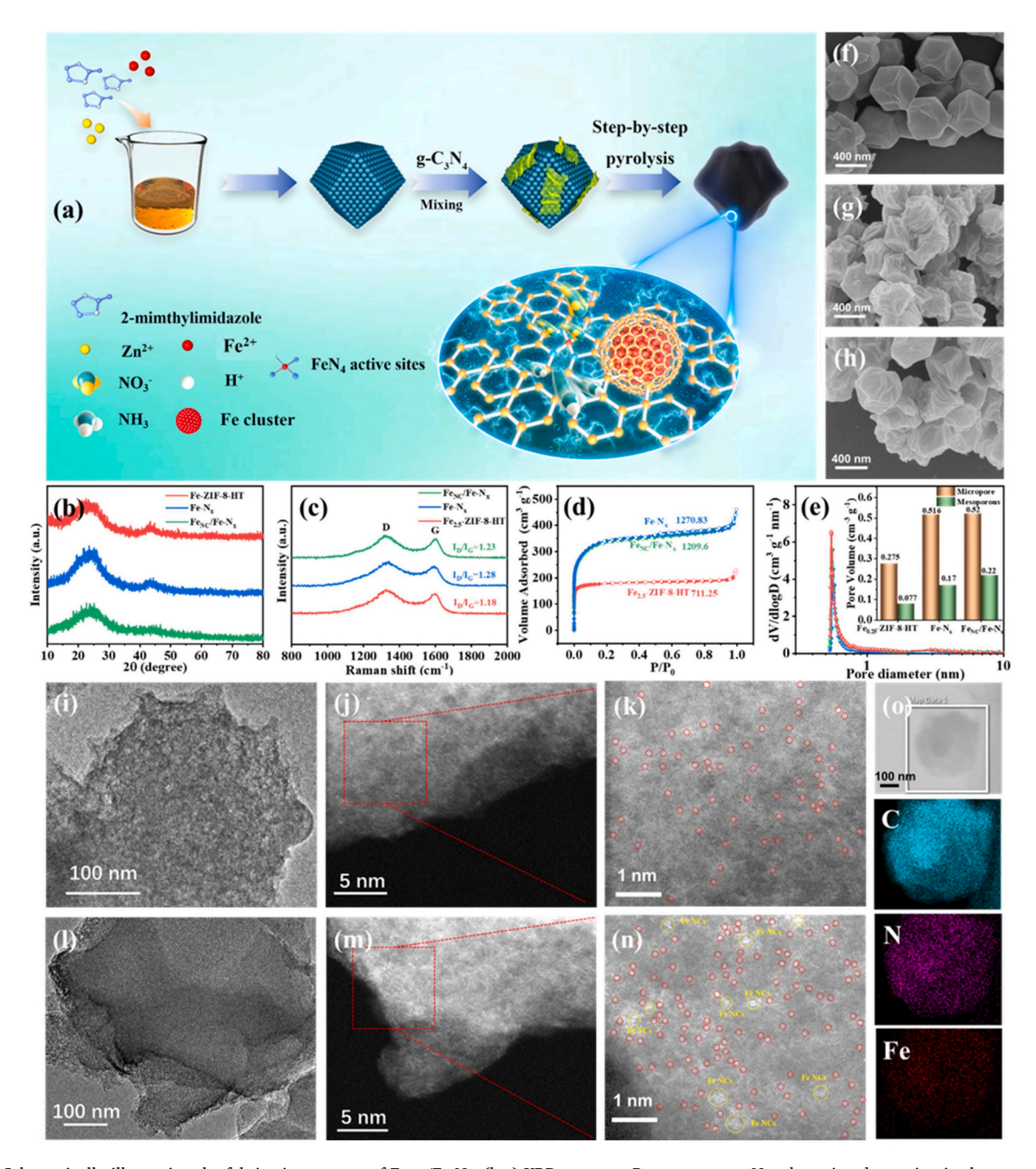


Fig. 1. (a) Schematically illustrating the fabrication process of $Fe_{NC}/Fe-N_x$. (b-e) XRD patterns, Raman spectra, N_2 adsorption-desorption isotherms, pore-size distribution plots and corresponding *meso*/microporous volumes of the as-prepared samples. (f - h) SEM images of $Fe_{2.5}$ -ZIF-8-HT, $Fe-N_x$ and $Fe_{NC}/Fe-N_x$. (i-k) TEM images and atomic resolution HAADF-STEMs of $Fe_{NC}/Fe-N_x$. (o) Corresponding mapping images of $Fe_{NC}/Fe-N_x$.

higher specific surface area in comparison to Fe_{2,5}-ZIF-HT (711.25 m² g⁻¹). The pore distribution plots (Fig. 1e) illustrate that the majority of pores in the as-prepared samples are situated within the micropore range. More than that, Fe_{NC}/Fe-N_x and Fe-N_x have similar micropore and mesoporous volumes, which are 0.516/0.52 cm³ g⁻¹ for micropore and 0.17/0.22 cm³ g⁻¹ for mesoporous (Fig. 1e inset), the values are twice as many as Fe_{2.5}-ZIF-8-HT, which could be caused by the decomposition of g-C₃N₄ to form NH₃ or CO₂, and then etching carbon matrix. The high micro/mesoporous and specific surface area can help to increase number of exposed active sites and enhance mass/electro transfer [46].

Subsequently, the morphology of the as-made samples were observed via SEM images. ZIF-8 and Fe-ZIF-8 exhibit a regular dodecahedron (Fig. S2a, b), whereas g-C₃N₄ with a lamellar stack is supported on Fe-ZIF-8 (Fig. S2c, d). Fig. 1f shows that Fe_{2.5}-ZIF-8-HT still keeps the dodecahedron structure with a slight reduction in size due to the decomposition of 2-MIM. Meanwhile, the surface of Fe-N_x (Fig. 1g) and Fe_{NC}/Fe-N_x (Fig. 1h) became rough with many wrinkles, exhibiting dried plums-like morphology. Moreover, in Fig. S3, one can find that the dodecahedron structure is collapsed as the amount of g-C₃N₄ increases.

TEM images (Fig. 1i, l) were carried out to analyze the morphology and structure of as-made samples. No discernible nanoparticles can be observed on the surface of Fe-N_x and $\text{Fe}_{NC}/\text{Fe-N}_x$, which corroborates the results obtained from the XRD analysis. The atomic resolution HAADF-STEM was employed to confirm the presence of Fe_{NC} and Fe-N_x in as-prepared samples. In Fig. 1j, k, there is the existence of numerous isolated bright spots (red circle) in Fe-N_x, which provides compelling

evidence that Fe exists predominantly as a single atom. Compared with Fe-N_x, Fig. 1m, n reveal the presence of two distinct types of Fe species in Fe_{NC}/Fe-N_x: Fe atoms (red circles) scattered independently over the carbon support and Fe_{NC} (yellow circles) located near the Fe atoms. The results presented above demonstrate the successful preparation of Fe-N_x and Fe_{NC}/Fe-N_x. The EDS mapping images (Fig. 1o) were obtained to analyze the distribution of elements in Fe_{NC}/Fe-N_x. The results show that the C, N and Fe elements are uniformly distributed across the Fe_{NC}/Fe-N_x. The corresponding contents are evaluated using EDS spectrum (Fig. S4), which indicate that the content of C, O, N and Fe elements are 68.23, 13.70, 9.88 and 8.19 wt%, respectively. Considering that EDS measurement is a surface testing technique, ICP-OES (Table S1) test was used to further analyze the Fe content in the sample, the results show that the Fe contents in Fe_{NC}/Fe-N_x and Fe-N_x are about 5.2 and 3.1 wt%, respectively.

The electronic structure and coordination environment were investigated through the utilization of XAS measurements. The Fe K-edge XANES spectra (Fig. 2a) show that the near-edge absorption energy of Fe-N_x is between FeO and Fe₂O₃, indicating that the oxidation state of Fe in Fe-N_x is between +2 and +3, while the near-edge absorption energy of Fe_{NC}/Fe-N_x is lower than that that of Fe-N_x due to the exist of Fe_{NC}. To obtain additional coordination data, the corresponding Fourier-transformed (FT) k³-weighted extended X-ray absorption fine structure (EXAFS) spectra (Fig. 2b) were subjected to analysis. The Fe-N_x sample exhibit a dominant peak at approximately 1.6 Å, which is attributed to Fe-N coordination within the first shell [47]. Additionally, no Fe—Fe peaks were observed at around 2.2 Å, further corroborating the notion

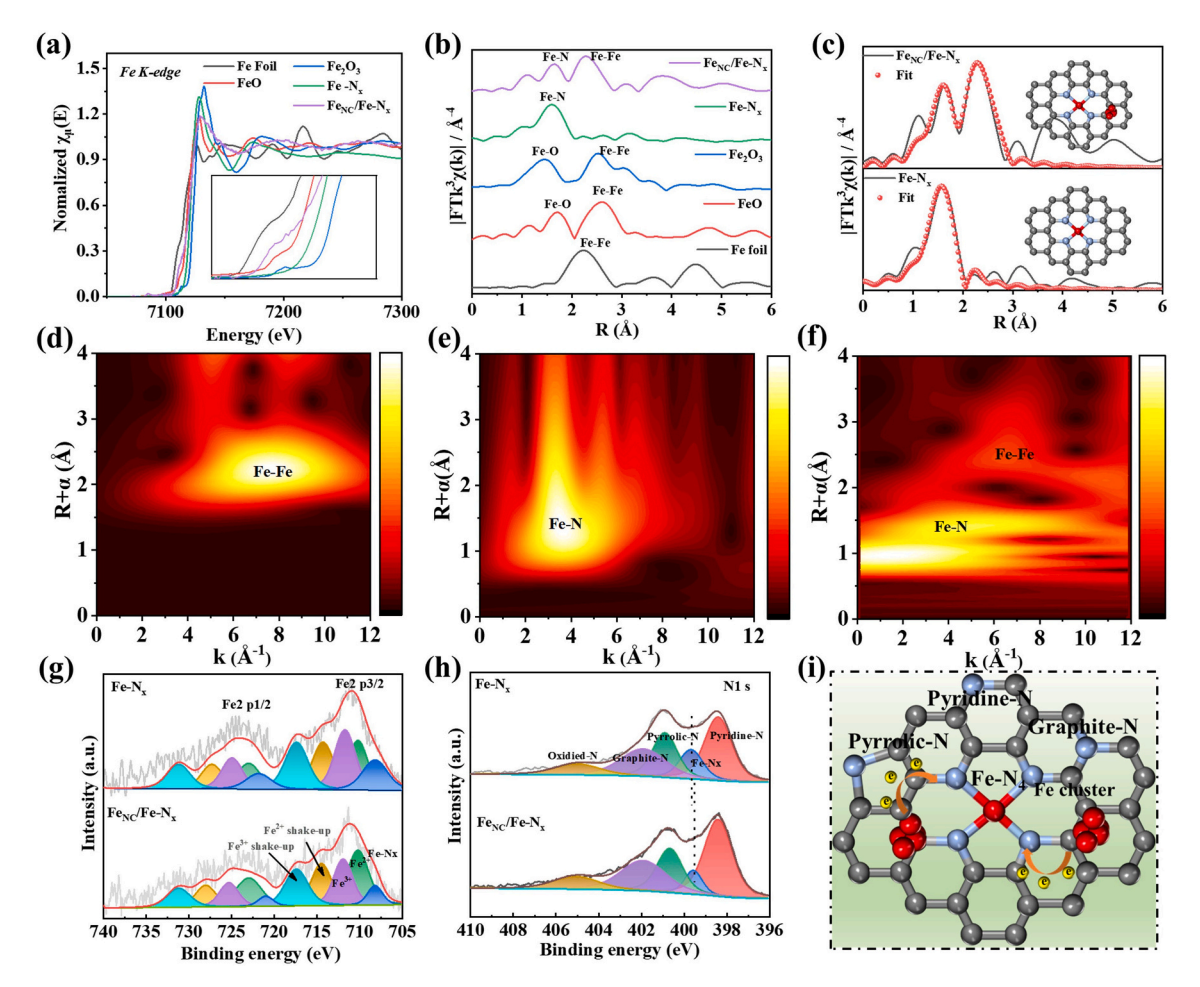


Fig. 2. (a) XANES spectra of the Fe K-edge. (b) FT k^3 -weighted $\chi(k)$ -function of the EXAFS spectra at the Fe K-edge. (c) Fitting results of the EXAFS spectra at R space. (d-f) Wavelet transform (WT) plots of the Fe K-edge. (g, i) Fe 2p and N 1 s spectra of Fe-N_x and Fe_{NC}/Fe-N_x. (h) Schematic drawing of the charge interaction between Fe_{NC} and Fe-N_x.

that the Fe exists as a single atom. As for the Fe $_{NC}$ /Fe- N_x , the presence of two dominant peaks attributed to Fe-N and Fe—Fe well confirms the exists of Fe- N_x and Fe $_{NC}$.

In addition, we employed EXAFS fitting to ascertain the structural parameters and quantify the chemical configuration of Fe atoms in FeNC/Fe-Nx and Fe-Nx. The pertinent results are presented in Fig. 2c, S5 and Table S2. All R-factors are less than 0.02, thereby attesting to the reliability of the data. The fitting results indicate that the coordination numbers (CN) of Fe-N and Fe—Fe in FeNC/Fe-Nx are approximately 4 and 3, respectively, as shown in Fig. 2c inset. In order to clearly observe the bonding in as-prepared samples, WT-EXAFS patterns (Fig. 2d-f and S6) were performed. There is only one intensity maximum in Fe-Nx at around 4.0 Å $^{-1}$, which is close to the value of Fe-N bond in literature. However, there are two maximum intensities in FeNC/Fe-Nx, corresponding to Fe-N and Fe—Fe bonds, respectively. The results further confirm we successfully prepared FeNC/Fe-Nx electrocatalysts.

The full XPS spectrum (Fig. S7a) exhibits three distinct peaks, corresponding to C 1 s (298 eV), N 1 s (400 eV) and O 1 s (530 eV), respectively. In addition, a minor peak associated with Fe 2p can be observed at approximately 710 eV (Fig. S7a inset). As illustrated in Fig. S7b, the C 1 s spectrum exhibits four distinct peaks, which are attributed to C=C/C-C, C-N/C-O, O-C=O, and C 1 s plasmon, in that order [48]. In the Fe 2p spectra (Fig. 2g), a distinct peak corresponding to Fe—N is discernible in both Fe-N_x and Fe_{NC}/Fe-N_x, which provides further evidence that the iron atoms have been successfully incorporated into the carbon substrate [49]. The N 1 s spectra (Fig. 2h) provide another evidence to support the conclusion, the pyridine-N, Fe-N_x, Pyrrolic-N, Graphitic-N and oxidized N can be observed in both Fe-N_x and Fe_{NC}/Fe-N_x [50]. It is noteworthy that the binding energy (BE) of Fe-N_x in Fe_{NC}/Fe-N_x exhibits a negative shift of 0.15 eV in comparison to Fe-

 N_x . This observation suggests that Fe_{NC} can influence the electronic structure of $Fe-N_x$, resulting a charge transfer from Fe_{NC} to $Fe-N_4$ (Fig. 2i), which may contribute to regulating the performance of $Fe-N_x$.

The NO₃RR electroactivity of the as-prepared samples is evaluated in a H-shaped electrolytic cell through a three-electrode system (Fig. S8). Fig. 3a illustrates that the Fe_{NC}/Fe-N_x in a 0.50 M NaNO₃/0.10 M K₂SO₄ mixed electrolyte exhibited a higher current density (j) compared to the 0.10 M K₂SO₄ electrolyte at the same potential. This suggests that NO₃ could be reduced by the Fe_{NC}/Fe-N_x. The EIS results (Fig. S9 and Table S3) show that the R_{ct} in 0.50 M NaNO₃/0.10 M K₂SO₄ mixed electrolyte is lower than that of in 0.10 M K₂SO₄, indicating that charge transfer occurs with greater ease in the mixed electrolyte. Moreover, the LSV curves (Fig. 3b) demonstrate that the $Fe_{NC}/Fe-N_x$ composite exhibits superior performance compared to Fe_{2.5}-ZIF-8-HT and Fe-N_x. As illustrated in Fig. 3c, Tafel plots of Fe_{NC}/Fe-N_x reveal a more rapid NO₃RR kinetic with a diminished Tafel slope of 208 mV dec⁻¹ in comparison to Fe-N_{x} (240 mV dec^{-1}) and Fe-ZIF-8-HT (527 mV dec^{-1}). This is attributed to the presence of a rich micro/mesoporous structure and an optimized electronic configuration. To eliminate the influence of the electrochemical surface area (ECSA), the ECSA normalized LSV curves are also performed in Fig. S10, where the Fe_{NC}/Fe-N_x still show the better NO₃RR performance than that of Fe-N_x, indicating that introduction of Fe_{NC} enhance the intrinsic electroactivity of Fe-N_x.

In order to analyze the product selectivity, the chronoamperometry (i-t) curves of $Fe_{NC}/Fe-N_x$ were performed in $K_2SO_4+NaNO_3$ mixed electrolyte at a series of potentials (-0.60--1.10 V vs. RHE) (Fig. 3d), and the generated NH_3 and NO_2^- products were then quantified by correlative calibration ultraviolet-visible (UV–Vis) curves (Fig. S11 and S12). Fig. S13a and b exhibit the UV–Vis curves of $Fe_{NC}/Fe-N_x$ for generated NH_4^+ and NO_2^- after i-t-tests at different potentials. Based on

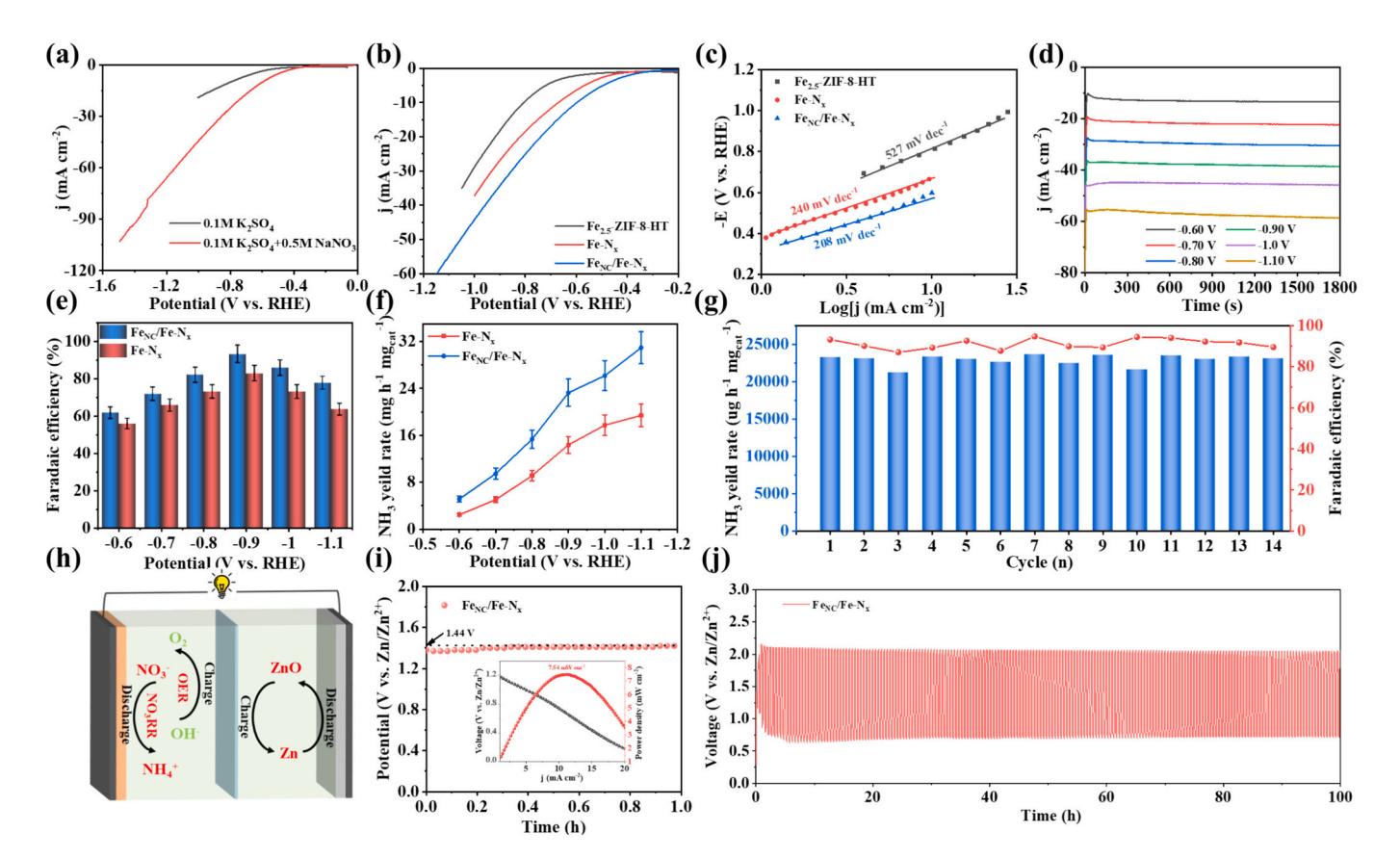


Fig. 3. (a) LSV curves of $Fe_{NC}/Fe-N_x$ in 0.10 M K_2SO_4 electrolyte and 0.50 M $NaNO_3/0.10$ M K_2SO_4 mixed electrolyte. (b) LSV curves of the as-prepared samples in 0.50 M $NaNO_3/0.10$ M K_2SO_4 mixed electrolyte. (c) Corresponding Tafel plots. (d) I-t curves of $Fe_{NC}/Fe-N_x$ at different fixed potentials. (e) Fe_{NH3} at each given potential. (f) Y_{NH3} at each given potential. (g) The cycling tests at -0.90 V vs. RHE, (catalyst loading: 0.4 mg cm $^{-2}$). (h) Schematic diagram of the Zn-NO $_3$ battery. (i) Open-circuit voltage and polarization/power density pots of $Fe_{NC}/Fe-N_x$. (j) Long-term charge and discharge cycling curves of $Fe_{NC}/Fe-N_x$ at 2.0 mA cm $^{-2}$.

the correlative calibration curves, it is easy to find that $Fe_{NC}/Fe-N_x$ displays the highest FE of NH $_3$ (FE $_{NH3}$) (93.6 %) at -0.9 V vs. RHE (Fig. 3e), while the FE of NO $_2^-$ was lower than 2.5 % at whole test potentials (Fig. S14), indicating $Fe_{NC}/Fe-N_x$ has an excellent selectivity for NH $_3$. Furthermore, the FE $_{NH3}$ of Fe-N $_x$ was also calculated by the same way. The correlative UV–Vis curves are shown in Fig. S15 and S16. The highest FE $_{NH3}$ was only 82 % at -0.9 V vs. RHE. Fig. 3f shows the yield rate of NH $_3$ (Y $_{NH3}$), and it is gradually going up as the negative potential increases. The Y $_{NH3}$ of Fe $_{NC}/Fe-N_x$ reaches 30.87 mg h $^{-1}$ mg $_{cat}^{-1}$ at -1.10 V vs. RHE, a value that is higher than that of Fe-N $_x$ (19.83 mg h $^{-1}$ mg $_{cat}^{-1}$). This finding provides favorable evidence that the Fe $_{NC}$ modification enhances the performance of NO $_3$ RR. As shown in Fig. S17, the high FE $_{NH3}$ and Y $_{NH3}$ were comparable to advanced NO $_3$ RR electrocatalysts have been reported in the literatures [25,51–56].

Additionally, the good durability of $Fe_{NC}/Fe-N_x$ in NO_3RR is well proved by the 14 times cycling tests at -0.9 V. (Fig. 3g). The corresponding V-t curves and absorption curves are shown in Fig. S18 a, b. To

ascertain the reason for the excellent stability, TEM, HAADF-STEM and XPS measurements were conducted to observe the structure and surface composition of $\text{Fe}_{\text{NC}}/\text{Fe-N}_x$ after long-term NO_3RR test. As illustrated in Fig. S19a and b, the morphology of $\text{Fe}_{\text{NC}}/\text{Fe-N}_x$ remains stable, and the Fe_{NC} and Fe single atom can also be discerned with clarity. The N 1 s and Fe 2p spectra (Fig. S20a, b) also display a peak associated with the Fe-Nx species after NO_3RR test. Based on the preceding analysis, it can be inferred that the stable structure and composition of $\text{Fe}_{\text{NC}}/\text{Fe-N}_x$ contribute to the excellent NO_3RR stability.

In order to further verify that the N in NH₃ originates from NO₃RR, a ^{15}N isotope labeling experiment was conducted by employing a Na $^{15}\text{NO}_3$ solution. Subsequently, the products obtained from this experiment are subject to qualitative analysis via ^{1H}NMR . As illustrated in Fig. S21, the ^{1H}NMR spectrum of Na $^{15}\text{NO}_3$ solution, following 1800-s test at -0.90 V vs. RHE, displays characteristic doublet peaks at chemical shifts $\delta\approx6.83$ and 7.02 ppm, which are corresponding to $^{15}\text{NH}_4^+$. In concast, the ^{1H}NMR spectrum without N 15 isotope labeling presents a typical triplet

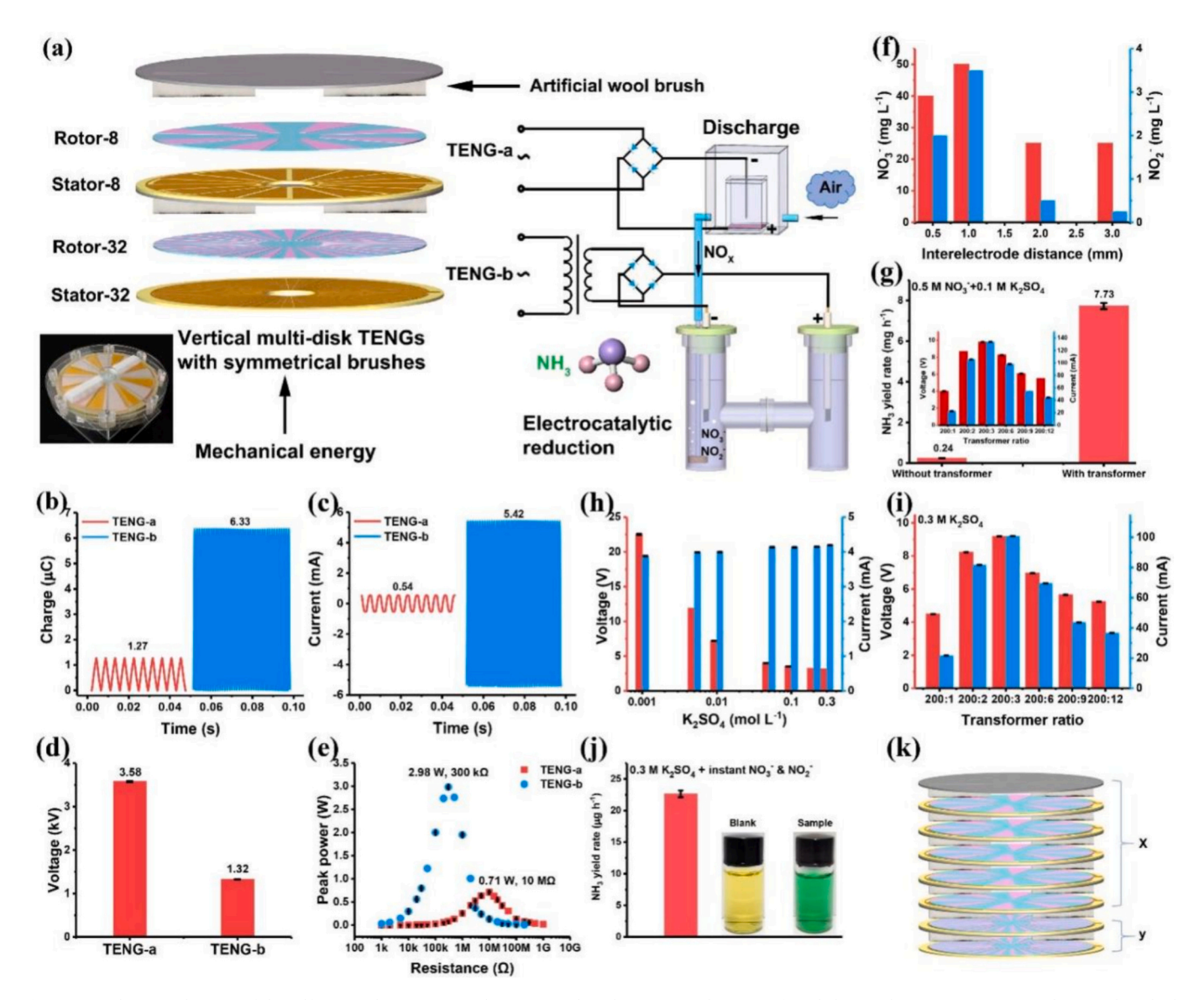


Fig. 4. (a) Schematic diagram of the self-powered ammonia synthesis system based on TENGs. (b-e) Transferred charge, short-circuit current, voltage under a high-resistance (1 $G\Omega$) condition, and peak power of TENG-a and TENG-b. (f) Concentration of NO_3^- and NO_2^- generated from the discharge device driven by TENG-a. (g) Voltage and current of the electrolytic cell driven by TENG-b at different transformer ratios and NH_3 yield rate driven by TENG-b without and with the optimum ratio (0.50 M NO_3^- /0.10 M K_2SO_4). (h) Voltage and current of the electrolytic cell driven by TENG-b at different concentrations of K_2SO_4 . (i) Voltage and current of the electrolytic cell driven by TENG-b at different transformer ratios. (j) NH_3 yield rate generated by self-powered synthesis from air. (k) Schematic diagram of reasonable quantity ratio of TENG-b.

pattern with peaks at $\delta\approx7.02,~6.94,~and~6.85$ ppm, which can be attributed to $^{14}\text{NH}_4^+.$ The results provide compelling evidence that that NH $_3$ produced during the experiment actually came from the electrochemical NO $_3$ RR. Furthermore, we also analyze the ^{1H}NMR spectra of $^{15}\text{NH}_4\text{Cl}$ with different concentrations, and build the corresponding standard curve between area and concentration (Fig. S22a, b). Based on the standard curve, the generated NH $_3$ is quantified, the yield rates of NH $_3$ are 31.65 mg h $^{-1}$ mg $^{-1}_{cat}$ the value is close to the results of UV–vis absorption, suggesting the quantitative accuracy and reliability.

Given its high electroactivity and stability, $Fe_{NC}/Fe-N_x$ is an optimal cathode material for a $Zn-NO_3$ battery. Consequently, we assessed the performance of a $Zn-NO_3$ battery based on the $Fe_{NC}/Fe-N_x$, the corresponding battery device is shown in the Fig. 3h. Fig. 3i shows that the $Zn-NO_3$ battery possesses a high open-circuit voltage of 1.44~V. An examination of the power density and polarization of the $Zn-NO_3$ battery (Fig. 3i inset) reveals a high peak power density of $7.54~mW~cm^{-2}$, further suggesting the high NO_3RR electroactivity of $Fe_{NC}/Fe-N_x$. Then, we analyze the long-term charge and discharge cycling stability. As shown in Fig. 3j, the $Zn-NO_3$ battery exhibits an excellent cycling stability, the voltage gap between charge and discharge is almost change at $2.0~mA~cm^{-2}$ after 100~h cycling. These findings suggest that $Fe_{NC}/Fe-N_x$ can be employed as a perfect cathode material in a $Zn-NO_3$ battery.

To further explore the application potential of Fe_{NC}/Fe-N_x, a selfpowered NH3 synthesis system based on TENG technique was introduced [40]. Fig. 4a is the schematic diagram of the updated synthesis system. Symmetrical artificial wool brushes were added into noncontact-sliding freestanding mode multi-disk TENGs (TENG-a and TENG-b) for continuous charge acquisition by soft contact with rotors. The difference of these two TENGs is the number of electrode pairs. One is for a higher voltage-output, the other one is for a larger currentoutput. Fig. S23 clearly shows the photographs of their rotors and stators. TENG-a can directly achieve air discharge and get NO_x for NO₃ and NO2 electrolyte by simple rectification, meanwhile, TENG-b can synchronously supply enough voltage and electrons for the Fe_{NC}/Fe-N_x based electrocatalytic reaction under the circuit management of transformer and rectifier. Fig. 4b-e is the basic performance of TENG-a and TENG-b, in which the output characteristics of each kind of TENG are well displayed. The transferred charge achieved 1.27 μC and 6.33 μC, respectively. TENG-b has a better short-circuit current up to 5.42 mA, while TENG-a can direct output a higher voltage over 3.5 kV. As for the maximum peak power, TENG-a performs 0.71 W at the high-resistance of 10 M Ω , TENG-b possesses the advantage of lower matched resistance (300 k Ω) and a higher power value of 2.98 W.

Before running the whole system, we did some simulated experiments to verify that the two main parts, air discharge and electrocatalytic reduction, could work properly under the drive of TENGs. First, a group of needle-plate discharge devices with different interelectrode distances driven by TENG-a were tested. By a quick water-analysis-strips method, NO₃ and NO₂ from the cathode region are detected after 1 h discharge, and the results are shown in Fig. 4f. It is clear to see that at the distance of 1 mm, more NO₃ and NO₂ could be obtained. As for the electrocatalytic part, a larger current is better for the yield while meeting the voltage requirement. The diagram illustrated in Fig. 4g indicates that the optimum transformer ratio is 200:3 under the electrolyte condition of $0.50~M~NO_3^-/0.10~M~K_2SO_4$ driven by TENG-b. At the best ratio, the NH3 yield rates after 1 h reaction without or with transformer are 0.24 and 7.73 mg h⁻¹, respectively. The results demonstrate that the electrocatalytic system works well with the TENG power, and a suitable transformer is a good tool for high yield. Since the electrolytes for NH3 synthesis in the system are got from air discharge, the optimizations of neutral-electrolyte concentration and following transformer ratio were also done (Fig. 4h and i). The concentration of 0.30 M K₂SO₄ and the ratio of 200:3 was selected, a power over 9 V and 100 mA can be obtained from TENG-b. Finally, under all optimized conditions, the whole system ran for 2 h. The NH₃ yield rate is 22.66 μ g h⁻¹ (Fig. 4j), which is as 9.4 times high as that of the previous work that synthesizing

 $\rm NH_3$ from air [40]. Compared with the results directly using nitrate as the electrolyte, both with electrochemical workstation power and TENG power, we realize that the concentration of $\rm NO_3^-$ is a determinant for better yield in our self-powered synthesis system. Therefore, as shown in Fig. 4k, a reasonable quantity ratio of TENG-a to TENG-b is an important factor worth considering and calculating for future practical applications. Moreover, a more sophisticated and controllable circuit management is another necessary for the future work.

To better investigate the mechanism of Fe clusters to NO₃RR, DFT simulations were conducted. The optimized structures of Fe-N_x and Fe_{NC}/Fe-N_x are illustrated in Fig. 5a, S24-26. Additionally, the molecular orbitals of the NO₃RR intermediates were calculated to provide a clearer understanding of the reaction mechanism (Fig. 5b). It should be mentioned that the molecular orbitals with σ or σ^* symmetry are not involved in further bonding because they are localized between atoms and exhibit minimal overlap with the orbitals of the active sites. Correspondingly, the spin-resolved projected density of states (PDOS) of the *d* orbitals for both models were calculated (Fig. 5c). In general, the dz^2 and dx^2-y^2 orbitals are less occupied than the dxz, dyz, and dxy orbitals, as evidenced by the higher PDOS values above the Fermi level. Specifically, the electron occupancies of dz^2 , dxz, and dyz, which overlap with the intermediate orbitals due to symmetry matching [57,58], were calculated and are presented in Fig. 5d. Notably, Fe_{NC}/Fe-N_x exhibits higher electron occupancy in the dz^2 orbital, indicating an elevated spin state. These results further confirm that the presence of Fe nanoclusters significantly alters the electronic structure of the Fe-N_x active sites.

The dz^2 orbital is oriented along the axis perpendicular to the Fe-N_x plane, enabling strong axial interactions with adsorbates situated directly atop the Fe center. This orbital geometry makes dz^2 particularly important for the adsorption and activation of NO₃RR intermediates such as NO₃, NO₂, and HNO. In addition, the dxz and dyz orbitals contribute through lateral π -type interactions with the intermediate orbitals. Together, these three orbitals (dz^2 , dxz, and dyz) form the dominant bonding channels between the Fe active sites and the intermediates.

Subsequently, the BO between the active sites and intermediates was calculated using the formula $BO = (n_b-n_{ab})/2$, where n_b and n_{ab} represent the number of electrons in bonding and anti-bonding states, respectively. BO serves as an indicator of bonding strength, a larger BO value corresponds to a stronger bonding and, consequently, a greater adsorption ability of the active sites. As shown in Fig. 5e, Fe_{NC}/Fe-N_x exhibits smaller BO values for all studied intermediates during NO₃RR, indicating a reduction in adsorption strength following the introduction of Fe nanoclusters. Furthermore, as for the energetic priority in the whole NO₃RR reaction process, it is determined by the free energy of the RDS. As displayed in Fig. 5f, the RDS of the NO₃RR reaction is the conversion of *HNO to *N, which involves the desorption of the OH radical. For the Fe-Nx structure, the RDS free energy of NO3RR was calculated to be 2.88 eV. However, the free energy decreased to 2.77 eV on Fe_{NC}/Fe-N_x when the Fe_{NC} were combined, indicating that the introduction of Fe_{NC} made NO₃RR more thermodynamically favorable. These findings align with the spin-state analysis, indicating that the reduced adsorption strength due to Fe nanoclusters could effectively facilitate desorption steps, thus enhancing the overall reaction kinetics.

4. Conclusion

In summary, we have successfully prepared carbon cage supported Fe $_{\rm NC}$ modified Fe-N $_{\rm x}$ (Fe $_{\rm NC}$ /Fe-N $_{\rm x}$) as an efficient NO $_3$ RR electrocatalyst by simple pyrolysis of Fe-ZIF-8/g-C $_3$ N $_4$. Characterizations and theoretical calculations indicate that the exist of g-C $_3$ N $_4$ increase the specific surface area and pore volumes of Fe $_{\rm NC}$ /Fe-N $_{\rm x}$ to improve the number of active site and facilitate mass transfer. The introduction of Fe $_{\rm NC}$ enriches the electron filling of d-band of Fe-N $_{\rm x}$ species to regulate their spin state, thereby lowering the energy barrier of RDS in NO $_3$ RR. So, Fe $_{\rm NC}$ /Fe-N $_{\rm x}$ exhibits an enhanced NO $_3$ RR performance with high FE and yield rate of

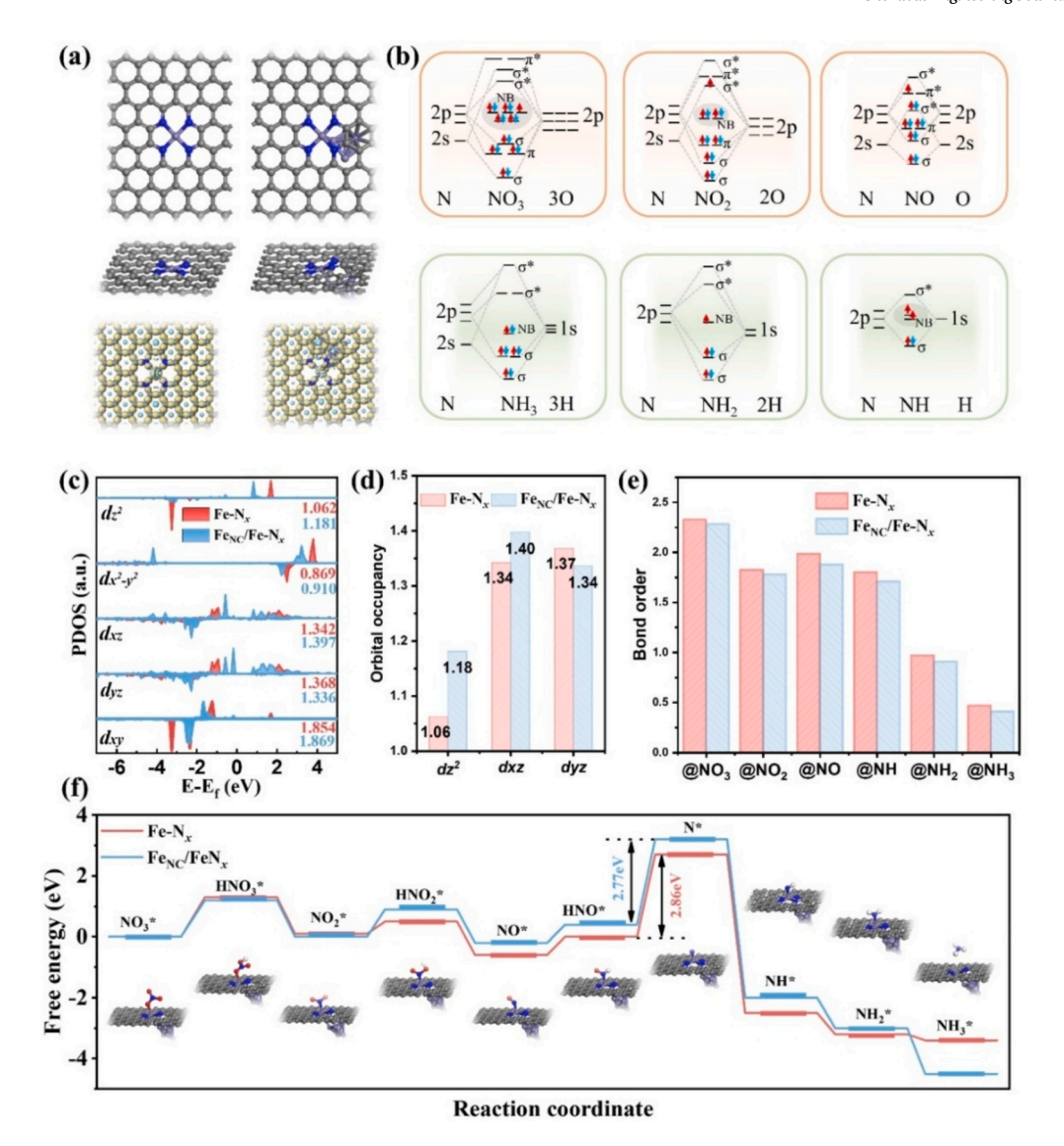


Fig. 5. (a) Schematic models of Fe-N $_x$ and Fe $_{NC}$ /Fe-N $_x$. (b) Molecular orbital diagrams of the NO $_3$ RR intermediates. (c) Spin-resolved PDOS of Fe-N $_x$ and Fe $_{NC}$ /Fe-N $_x$. (d) Calculated orbital occupancies according to the spin-resolved PDOS. (e) Calculated bond orders of the NO $_3$ RR intermediates on Fe-N $_x$ and Fe $_{NC}$ /Fe-N $_x$. (f) Free energy diagrams of the NO $_3$ RR intermediates from NO $_3$ * to NH $_3$ * on Fe-N $_x$ and Fe $_{NC}$ /Fe-N $_x$ and structural optimized models of NO $_3$ RR intermediates on Fe $_{NC}$ /Fe-N $_x$.

 NH_3 , which are 93.6 % at -0.90~V vs. RHE and 30.87 mg h^{-1} mg $_{\rm cat}^{-1}$ at -1.10~V vs. RHE, respectively. Based on the high electroactivity and stability, $Fe_{NC}/Fe-N_x$ is a very good choice for powerful Zn- NO_3 battery. Furthermore, the high selectivity making it a competitive catalyst for NH_3 synthesis. And such an advantage was well shown in a TENG-driven air-sourced NH_3 synthesis system. Both of the above applications demonstrate the remarkable practical value of $Fe_{NC}/Fe-N_x$. Our findings provide a good guidance of optimizing SACs for better NO_3RR performance. Furthermore, the studies also demonstrate the feasibility of an intelligent and sustainable methodology for future applications.

CRediT authorship contribution statement

Bingyi Song: Writing – original draft, Formal analysis, Data curation. Dong Xiang: Software, Formal analysis. Chengjie Chen: Formal analysis, Data curation. Jinchang Xu: Writing – original draft, Formal analysis. Yangshuai Ma: Formal analysis. Linjing Yang: Formal analysis. Ming-Hsien Lee: Software. DengkeZhao: Writing – review & editing, Writing – original draft, Supervision, Funding acquisition, Formal analysis, Data curation. Kai Han: Writing – review & editing, Writing – original draft, Formal analysis, Data curation. Nan Wang:

Writing – review & editing, Funding acquisition, Formal analysis.

Declaration of competing interest

The authors declare that they have no known competing financial interests or personal relationships that could have appeared to influence he work reported in this paper.

Acknowledgements

This work was supported by the National Natural Science Foundation of China (22109051, 22209056, 22075102, 22005120, 21576301 and 51973244), the Guangdong Basic and Applied Basic Research Foundation (2023A1515010270) and the Science and Technology Planning Project of Guangzhou, China (Grant No. 201605030008, SL2024A04J00672, 2025A04J5167), the Key Research & Development and Promotion Projects in Henan Province (242102241033).

Appendix A. Supplementary data

Supplementary data to this article can be found online at https://doi.

org/10.1016/j.cej.2025.166374.

Data availability

No data was used for the research described in the article.

References

- [1] H. Xu, Y. Ma, J. Chen, W.-x. Zhang, J. Yang, Electrocatalytic reduction of nitrate a step towards a sustainable nitrogen cycle, Chem. Soc. Rev. 51 (2022) 2710–2758.
- [2] G. Gan, G. Hong, W. Zhang, Active hydrogen for electrochemical ammonia synthesis, Adv. Funct. Mater., n/a 2401472.
- [3] X.-Y. Ji, K. Sun, Z.-K. Liu, X. Liu, W. Dong, X. Zuo, R. Shao, J. Tao, Identification of dynamic active sites among Cu species derived from MOFs@CuPc for electrocatalytic nitrate reduction reaction to ammonia, Nano-Micro Lett. 15 (2023) 110.
- [4] J. Zhou, M. Wen, R. Huang, Q. Wu, Y. Luo, Y. Tian, G. Wei, Y. Fu, Regulating active hydrogen adsorbed on grain boundary defects of nano-nickel for boosting ammonia electrosynthesis from nitrate, energy. Environ. Sci. 16 (2023) 2611–2620.
- [5] Q. Peng, D. Xing, L. Dong, Y. Fu, J. Lu, X. Wang, C. Wang, C. Guo, Electrochemical nitrate reduction for ammonia production: amorphous or crystalline oxidized copper catalyst? J. Mater. Chem. A 12 (2024) 8689–8693.
- [6] L. Wang, Y. Liu, H. Wang, T. Yang, Y. Luo, S. Lee, M.G. Kim, T.T.T. Nga, C.-L. Dong, H. Lee, Oxygen-bridged vanadium single-atom dimer catalysts promoting high faradaic efficiency of Ammonia Electrosynthesis, ACS Nano 17 (2023) 7406–7416.
- [7] Y. Sun, X. Li, Z. Wang, L. Jiang, B. Mei, W. Fan, J. Wang, J. Zhu, J.-M. Lee, Biomimetic design of a dynamic M-O-V pyramid electron bridge for enhanced nitrogen electroreduction, J. Am. Chem. Soc. 146 (2024) 7752–7762.
- [8] H. Zhang, K. Fang, J. Yang, H. Chen, J. Ning, H. Wang, Y. Hu, Strategies and applications of electrocatalytic nitrate reduction towards ammonia, Coord. Chem. Rev. 506 (2024) 215723.
- [9] Y. Han, J. Shang, S. Yin, R. Cao, J. Zhang, W. Jiang, G. Liu, Symmetry-breaking structure electrocatalysts for nitrate reduction to ammonia, Green Chem. 26 (2024) 8145–8160.
- [10] J. Yu, R.-T. Gao, X. Guo, N.T. Nguyen, L. Wu, L. Wang, Electrochemical nitrate reduction to ammonia on AuCu single-atom alloy aerogels under wide potential window, Angew. Chem. Int. Ed., n/a e202415975.
- [11] S. Zhang, D. Chen, P. Chen, R. Zhang, Y. Hou, Y. Guo, P. Li, X. Liang, T. Xing, J. Chen, Y. Zhao, Z. Huang, D. Lei, C. Zhi, Concurrent mechanisms of hot electrons and interfacial water molecule ordering in Plasmon-enhanced nitrogen fixation, Adv. Mater. 36 (2024) 2310776.
- [12] C. Zhang, Y. Zhang, R. Deng, L. Yuan, Y. Zou, T. Bao, X. Zhang, G. Wei, C. Yu, C. Liu, Enabling logistics automation in nanofactory: cobalt phosphide embedded metal–organic frameworks for efficient electrocatalytic nitrate reduction to ammonia, Adv. Mater. 36 (2024) 2313844.
- [13] C. Wang, Z. Liu, Q. Peng, D. Xing, T. Hu, F. Du, C. Li, R. Ma, H. Yang, C. Guo, Bimetallic Cu11Ag3 nanotips for ultrahigh yield rate of nitrate-to-ammonium, Angew. Chem. Int. Ed. 64 (2025) e202415259.
- [14] W. Chen, X. Yang, Z. Chen, Z. Ou, J. Hu, Y. Xu, Y. Li, X. Ren, S. Ye, J. Qiu, J. Liu, Q. Zhang, Emerging applications, developments, prospects, and challenges of electrochemical nitrate-to-ammonia conversion, Adv. Funct. Mater. 33 (2023) 2300512
- [15] Y. Yao, X. Wei, H. Zhou, K. Wei, B. Kui, F. Wu, L. Chen, W. Wang, F. Dai, P. Gao, N. Wang, W. Ye, Regulating the d-Band center of metal-organic frameworks for efficient nitrate reduction reaction and zinc-nitrate battery, ACS Catal. 14 (2024) 16205–16213.
- [16] F. Du, J. Yao, H. Luo, Y. Chen, Y. Qin, Y. Du, Y. Wang, W. Hou, M. Shuai, C. Guo, A Cu loaded NiFe layered double hydroxide bifunctional electrocatalyst with a coupled interface structure for both the nitrate reduction reaction and oxygen evolution reaction, Green Chem. 26 (2024) 895–903.
- [17] A. Aminu, B.M. Pirzada, S.H. Talib, J. Shaya, I. Yildiz, S. Mohamed, A. Qurashi, Fe foam supported FeVO4 nanoparticles for electrochemical nitrogen fixation at ambient conditions, Nano Res. Energy 4 (2025) e9120161.
- [18] L. Qiao, A. Zhu, D. Liu, K. An, J. Feng, C. Liu, K.W. Ng, H. Pan, In situ reconstructed Cu/β-Co(OH)₂ tandem catalyst for enhanced nitrate Electroreduction to Ammonia in ampere-level, Adv. Energy Mater. 14 (2024) 2402805.
- [19] S. Wang, H. Gao, L. Li, K.S. Hui, D.A. Dinh, S. Wu, S. Kumar, F. Chen, Z. Shao, K. N. Hui, High-throughput identification of highly active and selective single-atom catalysts for electrochemical ammonia synthesis through nitrate reduction, Nano Energy 100 (2022) 107517.
- [20] R. Zhu, Y. Qin, T. Wu, S. Ding, Y. Su, Periodic defect engineering of iron–nitrogen–carbon catalysts for nitrate electroreduction to ammonia, Small 20 (2024) 2307315.
- [21] E. Murphy, B. Sun, M. Rüscher, Y. Liu, W. Zang, S. Guo, Y.-H. Chen, U. Hejral, Y. Huang, A. Ly, I.V. Zenyuk, X. Pan, J. Timoshenko, B.R. Cuenya, E.D. Spoerke, P. Atanassov, Synergizing Fe₂O₃ nanoparticles on single atom Fe-N-C for nitrate reduction to Ammonia at industrial current densities, Adv. Mater. 36 (2024) 2401133.
- [22] J. Yang, H. Qi, A. Li, X. Liu, X. Yang, S. Zhang, Q. Zhao, Q. Jiang, Y. Su, L. Zhang, J.-F. Li, Z.-Q. Tian, W. Liu, A. Wang, T. Zhang, Potential-driven restructuring of cu single atoms to nanoparticles for boosting the electrochemical reduction of nitrate to Ammonia. J. Am. Chem. Soc. 144 (2022) 12062–12071.
- [23] J. Xian, S. Li, H. Su, P. Liao, S. Wang, Y. Zhang, W. Yang, J. Yang, Y. Sun, Y. Jia, Q. Liu, Q. Liu, G. Li, Electrocatalytic synthesis of essential amino acids from nitric

- oxide using atomically dispersed Fe on N-doped carbon, Angew. Chem. Int. Ed. 62(2023) e202304007.
- [24] C. Wang, Y. Zhang, H. Luo, H. Zhang, W. Li, W.-x. Zhang, J. Yang, Iron-based nanocatalysts for electrochemical nitrate reduction, Small Methods 6 (2022) 2200790
- [25] Z.-Y. Wu, M. Karamad, X. Yong, Q. Huang, D.A. Cullen, P. Zhu, C. Xia, Q. Xiao, M. Shakouri, F.-Y. Chen, J.Y. Kim, Y. Xia, K. Heck, Y. Hu, M.S. Wong, Q. Li, I. Gates, S. Siahrostami, H. Wang, Electrochemical ammonia synthesis via nitrate reduction on Fe single atom catalyst, Nat. Commun. 12 (2021) 2870.
- [26] L.-H. Xu, W. Liu, K. Liu, Single atom environmental catalysis: influence of supports and coordination environments, Adv. Funct. Mater. 33 (2023) 2304468.
- [27] S. Yin, R. Cao, Y. Han, J. Shang, J. Zhang, W. Jiang, G. Liu, Electrocatalysts with atomic-level site for nitrate reduction to ammonia, J. Energy Chem. 96 (2024) 642–668.
- [28] J. Wan, J. Yang, N. Yang, Y. Sun, C. Hu, Y. Zhao, X. Xu, H. Qi, X. Li, H. Zhang, Axial chlorine-induced symmetry-breaking Iron single-atom catalyst for electrochemical Ammonia synthesis, ACS Catal. 15 (2025) 4507–4518.
- [29] L. Liu, A. Corma, Bimetallic sites for catalysis: from binuclear metal sites to bimetallic nanoclusters and nanoparticles, Chem. Rev. 123 (2023) 4855–4933.
- [30] F. Wang, J. Yang, J. Li, Y. Han, A. Li, R. Xu, X. Feng, T. Wang, C. Tong, J. Li, Z. Wei, Which is best for ORR: single atoms, nanoclusters, or coexistence? ACS Energy Lett. 9 (2024) 93–101.
- [31] Z. Wang, X. Jin, R. Xu, Z. Yang, S. Ma, T. Yan, C. Zhu, J. Fang, Y. Liu, S.-J. Hwang, Z. Pan, H.J. Fan, Cooperation between dual metal atoms and nanoclusters enhances activity and stability for oxygen reduction and evolution, ACS Nano 17 (2023) 8622–8633.
- [32] H. Huang, D. Yu, F. Hu, S.-C. Huang, J. Song, H.-Y. Chen, L.L. Li, S. Peng, Clusters induced electron redistribution to tune oxygen reduction activity of transition metal single-atom for metal–air batteries, Angew. Chem. Int. Ed. 61 (2022) e202116068.
- [33] F.-R. Fan, Z.-Q. Tian, Z. Lin Wang, Flexible triboelectric generator, Nano Energy 1 (2012) 328–334.
- [34] Z.L. Wang, On Maxwell's displacement current for energy and sensors: the origin of nanogenerators, Mater. Today 20 (2017) 74–82.
- [35] C. Wu, A.C. Wang, W. Ding, H. Guo, Z.L. Wang, Triboelectric Nanogenerator: a Foundation of the Energy for the new era, Adv. Energy Mater. 9 (2019) 1802906.
- [36] Y. Jiang, X. Liang, T. Jiang, Z.L. Wang, Advances in triboelectric nanogenerators for blue energy harvesting and marine environmental monitoring, Engineering 33 (2024) 204–224.
- [37] Y. Li, X. Liu, Z. Ren, J. Luo, C. Zhang, C. Cao, H. Yuan, Y. Pang, Marine biomaterial-based triboelectric nanogenerators: insights and applications, Nano Energy 119 (2024) 109046.
- [38] J. Luo, W. Gao, Z.L. Wang, The triboelectric nanogenerator as an innovative technology toward intelligent sports, Adv. Mater. 33 (2021) 2004178.
- [39] M.-C. Wong, W. Xu, J. Hao, Microplasma-discharge-based nitrogen fixation driven by triboelectric Nanogenerator toward self-powered Mechano-nitrogenous fertilizer supplier, Adv. Funct. Mater. 29 (2019) 1904090.
- [40] K. Han, J. Luo, Y. Feng, L. Xu, W. Tang, Z.L. Wang, Self-powered electrocatalytic ammonia synthesis directly from air as driven by dual triboelectric nanogenerators, Energy Environ. Sci. 13 (2020) 2450–2458.
- [41] N. Xuan, C. Song, G. Cheng, Z. Du, Advanced triboelectric nanogenerator based self-powered electrochemical system, Chem. Eng. J. 481 (2024) 148640.
- [42] Y. Zhu, S. Ning, X. Yu, X. Niu, M. Chen, W. Zhou, D. Zhao, Z. Li, N. Wang, N. Li, L. Li, Cobalt nanoparticles encapsulated in iron and nitrogen co-doped urchin-like porous carbons as an efficient bifunctional oxygen reversible catalyst for Zn-air batteries, Chem. Eng. J. 436 (2022) 135191.
- [43] Y. Liu, X. Zhang, Z. Chen, X. Zhang, P. Tsiakaras, P.K. Shen, Electrocatalytic reduction of nitrogen on FeAg/Si for ammonia synthesis: a simple strategy for continuous regulation of faradaic efficiency by controlling H+ ions transfer rate, Appl. Catal. B Environ. 283 (2021) 119606.
- [44] Y. Liu, S. Huang, J. Lu, S. Niu, P.K. Shen, Z. Hu, P. Tsiakaras, S. Gao, Ni_{0.25}Cu_{0.25}Sn_{0.25} Nanometallic glasses as highly efficient catalyst for electrochemical nitrate reduction to Ammonia, Adv. Funct. Mater. 34 (2024) 2411325.
- [45] Y. Song, X. Song, X. Wang, J. Bai, F. Cheng, C. Lin, X. Wang, H. Zhang, J. Sun, T. Zhao, H. Nara, Y. Sugahara, X. Li, Y. Yamauchi, Two-dimensional metal-organic framework superstructures from ice-templated self-assembly, J. Am. Chem. Soc. 144 (2022) 17457-17467.
- [46] S.H. Lee, J. Kim, D.Y. Chung, J.M. Yoo, H.S. Lee, M.J. Kim, B.S. Mun, S.G. Kwon, Y.-E. Sung, T. Hyeon, Design principle of Fe-N-C Electrocatalysts: how to optimize multimodal porous structures? J. Am. Chem. Soc. 141 (2019) 2035–2045.
- [47] Y. Zhan, T. Zhao, X. Wu, X. Gao, R. Huang, Z. Zhang, P. Li, X. Guan, C. Chen, X. Liu, X. Tang, N. Wang, H. Meng, Strengthening the oxygen reduction stability and activity of single iron active sites via a simultaneously electronic regulation and structure design strategy, Appl. Catal. B: Environ. Energy 357 (2024) 124254.
- [48] S. Wu, X. Liu, H. Mao, J. Zhu, G. Zhou, J. Chi, Z. Wu, L. Wang, Unraveling the tandem effect of nitrogen configuration promoting oxygen reduction reaction in alkaline seawater, Adv. Energy Mater. 14 (2024) 2400183.
- [49] W. Niu, L. Li, X. Liu, N. Wang, J. Liu, W. Zhou, Z. Tang, S. Chen, Mesoporous N-doped carbons prepared with thermally removable nanoparticle templates: An efficient Electrocatalyst for oxygen reduction reaction, J. Am. Chem. Soc. 137 (2015) 5555–5562.
- [50] T. Najam, S.S.A. Shah, H. Yin, X. Xiao, S. Talib, Q. Ji, Y. Deng, M.S. Javed, J. Hu, R. Zhao, A. Du, X. Cai, Q. Xu, Second-shell modulation on porphyrin-like Pt single atom catalysts for boosting oxygen reduction reaction, Chem. Sci. 15 (2024) 18513–18523.

- [51] X. Zhao, Q. Geng, F. Dong, K. Zhao, S. Chen, H. Yu, X. Quan, Boosting the selectivity and efficiency of nitrate reduction to ammonia with a single-atom cu electrocatalyst, Chem. Eng. J. 466 (2023) 143314.
- [52] J. Zhao, X. Ren, X. Liu, X. Kuang, H. Wang, C. Zhang, Q. Wei, D. Wu, Zn single atom on N-doped carbon: highly active and selective catalyst for electrochemical reduction of nitrate to ammonia, Chem. Eng. J. 452 (2023) 139533.
- [53] W. Zhang, S. Zhan, J. Xiao, T. Petit, C. Schlesiger, M. Mellin, J.P. Hofmann, T. Heil, R. Müller, K. Leopold, M. Oschatz, Coordinative stabilization of single bismuth sites in a carbon–nitrogen matrix to generate atom-efficient catalysts for electrochemical nitrate reduction to ammonia, Adv. Sci. 10 (2023) 2302623.
- [54] X. Cheng, W. Shang, Y. Li, J. Hu, J. Guo, D. Cao, N. Zhang, S. Zhang, S. Song, T. Liu, W. Liu, Y. Shi, Unveiling structural evolution of Fe single atom catalyst in nitrate reduction for enhanced electrocatalytic ammonia synthesis, Nano Res 17 (2024) 6826–6832.
- [55] L. Yang, C. Wang, Y. Li, W. Ge, L. Tang, J. Shen, Y. Zhu, C. Li, Frustrated Lewis pairs on Zr single atoms supported N-doped TiO2-x catalysts for electrochemical nitrate reduction to Ammonia, Adv. Funct. Mater. 34 (2024) 2401094.
- [56] W.-J. Sun, L.-X. Li, H.-Y. Zhang, J.-H. He, J.-M. Lu, A bioinspired Iron-centered Electrocatalyst for selective catalytic reduction of nitrate to Ammonia, ACS Sustain. Chem. Eng. 10 (2022) 5958–5965.
- [57] Y. Sun, S. Sun, H. Yang, S. Xi, J. Gracia, Z.J. Xu, Spin-related electron transfer and orbital interactions in oxygen electrocatalysis, Adv. Mater. 32 (2020) 2003297.
- [58] J. Dai, Y. Tong, L. Zhao, Z. Hu, C.-T. Chen, C.-Y. Kuo, G. Zhan, J. Wang, X. Zou, Q. Zheng, W. Hou, R. Wang, K. Wang, R. Zhao, X.-K. Gu, Y. Yao, L. Zhang, Spin polarized Fe1—Ti pairs for highly efficient electroreduction nitrate to ammonia, Nat. Commun. 15 (2024) 88.